Structural Health Monitoring
http://shm.sagepub.com/

Sensing optical fiber installation study for crack identification using a stimulated Brillouin-based strain sensor

Michio Imai and Maria Feng
Structural Health Monitoring published online 23 April 2012
DOI: 10.1177/1475921712442440

Article

SHM Structural Health Monitoring

Structural Health Monitoring
0(0) 1–9

DOI: 10.1177/1475921712442440
shm.sagepub.com
SAGE

Sensing optical fiber installation study for crack identification using a stimulated Brillouin-based strain sensor

Michio Imai and Maria Feng

Abstract

Stimulated Brillouin-based optical fiber sensors have been receiving increasing attention in recent times because of their ability to measure distributed strain at high spatial resolution. This study presents a methodical approach for understanding the structural behavior from measured strain distribution. A stress-transferring model, focusing on the tip of a crack in concrete, with stress transfer from the host structure to the sensing segment on the attached fiber, was investigated. The loss of information due to the limited spatial resolution of the sensor was also analyzed. An experimental study using a notched concrete prism demonstrated the effectiveness of the proposed model for crack identification, allowing the study to leverage the stimulated Brillouin-based sensor to crack quantification as well as detection and localization.

Keywords

Stimulated Brillouin scattering, optical fiber sensor, strain measurement, distributed sensing, stress transfer

Introduction

Optical fiber sensors can measure structural information in terms of strain; however, except for discrete sensors, there is insufficient technical literature about simple models for the interpretation of strain data for the host structural behavior. Conventional Brillouin-based sensors have never been used for this stress-transferring problem, which usually requires higher accuracy discrete sensors, while it can be generally stated that error from Brillouin-based sensors is too large for such an application. For instance, short-gauge sensors, for example, fiber Bragg gratings and Fabry–Perot interferometers, have been used in studies of stress-transferring mechanisms.[1,2] A theoretical model of stress distribution based on force equilibria between various components (the host materials, protective coating, fiber core, and cladding) was introduced in a previous study over a short length of a Michelson white-light interferometer and was evaluated experimentally.[3] The study first took into account the effect of protective coating on the quantitative strain evaluation. From that study, another study simplified the stress-transferring model to be a function of the shear-lag parameter (which depends on geometry and stiffness) based on the classical force equivalent derivation.[4] A recent study analyzed the three-dimensional finite-element model of the surface-attached short-gauge sensor to improve it by considering the detailed geometry of the fiber and the adhesive.[5] Their assumptions included the boundary conditions of both ends of the short-gauge sensor, because there was no axial tensile force at the points. Accordingly, their findings are only directly relevant to an embedded short-length sensor where such a stress-transferring problem cannot be neglected in comparison to its high accuracy.

In recent decades, distributed optical fiber sensors have achieved significant technical advancements. When compared with conventional spontaneous Brillouin-based sensors, systems that employ stimulated Brillouin scattering for fully distributed strain measurement have shown encouraging performances. Their advancement in the field of spatial resolution

Department of Civil and Environmental Engineering, University of California, Irvine, CA, USA

Corresponding author:
Michio Imai, Department of Civil and Environmental Engineering, University of California, Irvine, CA 92697-2175, USA
Email: mimai@uci.edu

offers new possibilities for further applications, for example, crack identification (detection, localization, and quantification). However, few available theoretical analyses for distributed optical fiber sensors have been performed, whereas specific sensor-coating studies have been carried out into robust installation techniques and highly unified behavior, focused on surface-mounted and embedded sensors in a host structure.[6–8] More specifically, for gradual strain-change measurement, an analytical approach for extracting continuous strain profiles has been investigated.[9] Except for such gradual strain-distribution scenarios, stress-transferring mechanisms have not been substantially studied for distributed sensors. This article presents a strain-distribution model for severe strain-changing events, that is, cracking, and experimental results measured by Brillouin optical correlation domain analysis (BOCDA)–based strain sensors, one type of stimulated Brillouin-based optical fiber sensors.

Numerical model

Classical approach

To analyze the mechanical properties of fibrous materials, the classical approach, which introduces a shear-lag parameter to encapsulate both the effects of geometry and the relative stiffness of the system components, was considered. When a fiber having a radius r_f is surrounded by a material having a radius R, the shear-lag parameter is defined as follows (see Appendix 1 for nomenclature)[10]

$$n^2 = \frac{E_m}{E_f} \frac{1}{(1+\nu_m)\ln(R/r_f)} \tag{1}$$

where E_f is Young's modulus for the fiber, and E_m and ν_m represent Young's modulus and Poisson's ratio of the surrounding material, respectively.

Over the last two decades, with the development of discrete sensors, stress translating from optical fiber sensors has been investigated. To arrive at the governing equation (equation (11)), a number of lead-up equations are required, and these shall be presented here. Their presentation acts as a review of the analysis of finite-length cylindrical inclusions embedded in a surrounding material with an axially constant strain field.[4,5] As shown in Figure 1, the mean normal stress on the fiber can be described in terms of the shear stress acting on the outer fiber surface

$$\frac{\partial}{\partial z}\bar{\sigma}_z^f(z) = \frac{-2\tau_{rz}^f(r_f, z)}{r_f} \tag{2}$$

Introducing a free-body diagram of an infinitesimal element of the surrounding materials, the following

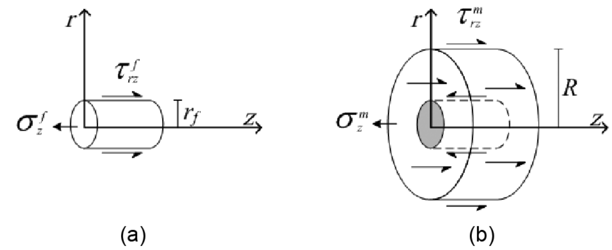

Figure 1. Stress-equivalent diagrams: (a) sensing fiber and (b) surrounding material.

equation is derived from the equivalence of forces in the z-direction

$$\frac{r^2 - r_f^2}{2}\frac{\partial}{\partial z}\bar{\sigma}_z^m(z) - \tau_{rz}^f(r_f, z)r_f + \tau_{rz}^m(r, z)r = 0 \tag{3}$$

Considering the interfacial force equivalence, the shear force on the outer surface of the fiber $\left(\tau_{rz}^f(r_f, z)\right)$ is equivalent to the shear force on the inner surface of the surrounding material $\left(\tau_{rz}^m(r_f, z)\right)$. Therefore, the following expression is derived from equations (2) and (3)

$$\tau_{rz}^m(r, z) = -\frac{r_f^2}{2r}\frac{\partial}{\partial z}\bar{\sigma}_z^f(z) - \frac{r^2 - r_f^2}{2r}\frac{\partial}{\partial z}\bar{\sigma}_z^m(z) \tag{4}$$

Assuming that the transverse stresses on the fiber and the coating are negligible, equation (4) can be expressed using stiffness and mean axial strains as follows

$$\tau_{rz}^m(r, z) = -\frac{E_f r_f^2}{2r}\left\{\frac{\partial}{\partial z}\bar{\varepsilon}_z^f(z) + \frac{r^2 - r_f^2}{r_f^2}\frac{E_m}{E_f}\frac{\partial}{\partial z}\bar{\varepsilon}_z^m(z)\right\} \tag{5}$$

Alternatively, the shear stress can be expressed in terms of the shear modulus, G_m, and the transverse and longitudinal displacements

$$\tau_{rz}^m(r, z) = G_m\left(\frac{\partial}{\partial r}\omega^m(r, z) + \frac{\partial}{\partial z}u^m(r, z)\right) \tag{6}$$

From equations (5) and (6), the following equation can be derived

$$\begin{aligned} G_m\left(\frac{\partial}{\partial r}\omega^m(r, z) + \frac{\partial}{\partial z}u^m(r, z)\right) = \\ -\frac{E_f r_f^2}{2r}\left\{\frac{\partial}{\partial z}\bar{\varepsilon}_z^f(z) + \frac{r^2 - r_f^2}{r_f^2}\frac{E_m}{E_f}\frac{\partial}{\partial z}\bar{\varepsilon}_z^m(z)\right\} \end{aligned} \tag{7}$$

In fact, most rigid polymers exhibit values of about 0.3 for Poisson's ratio. Since it can be assumed that the transverse (u-direction) displacement via the Poisson effect is less significant than the longitudinal

(ω-displacement) one, the second term in the left bracket of equation (7) is negligible. Therefore,

$$G_m \frac{\partial}{\partial r}\omega^m(r,z) = -\frac{E_f r_f^2}{2r}\left\{\frac{\partial}{\partial z}\overline{\varepsilon}_z^f(z) + \frac{r^2 - r_f^2}{r_f^2}\frac{E_m}{E_f}\frac{\partial}{\partial z}\overline{\varepsilon}_z^m(r,z)\right\} \tag{8}$$

Integrating from the interfacial boundary between the fiber and the coating to the outer surface of the coating leads to the following expression, which uses Young's modulus and Poisson's ratio instead of the shear modulus

$$\omega^m(R,z) - \omega^m(r_f,z) = -(1+\nu_m) \frac{E_f}{E_m}\ln\left(\frac{R}{r_f}\right)r_f^2\left\{\frac{\partial}{\partial z}\overline{\varepsilon}_z^f(z) + \frac{R^2 - r_f^2}{r_f^2}\frac{E_m}{E_f}\frac{\partial}{\partial z}\overline{\varepsilon}_z^m(r,z)\right\} \tag{9}$$

where

$$E_m = 2(1+\nu_m)G_m \tag{9a}$$

Moreover, differentiating equation (9) with respect to the z-direction yields the following

$$\varepsilon_z^m(R,z) - \varepsilon_z^f(z) = -(1+\nu_m) \frac{E_f}{E_m}\ln\left(\frac{R}{r_f}\right)r_f^2\left\{\frac{\partial^2}{\partial z^2}\overline{\varepsilon}_z^f(z) + \frac{R^2 - r_f^2}{r_f^2}\frac{E_m}{E_f}\frac{\partial^2}{\partial z^2}\overline{\varepsilon}_z^m(r,z)\right\} \tag{10}$$

Finally, the following expression can be derived using the shear-lag parameter (equation (1))

$$\varepsilon_z^m(R,z) + \left(\frac{R^2 - r_f^2}{n^2}\frac{E_m}{E_f}\right)\frac{\partial^2}{\partial z^2}\varepsilon_z^m(R,z) = \varepsilon_z^f(z) - \left(\frac{r_f^2}{n^2}\right)\frac{\partial^2}{\partial z^2}\varepsilon_z^f(z) \tag{11}$$

Development of numerical model

In this section, a numerical model suited to distributed optical fiber sensors with high spatial resolutions for crack identification is further developed. In addition to the classical strain-transferring model given in the previous section, it is necessary to add a model for the crack-induced strain condition. In this study, it is assumed that the strain distribution on the outer surface of the coating, $\varepsilon_z^m(R,z)$, is Gaussian, as Duck and LeBlanc[4] propose. The equation is a function of the position (z) and the full width at half maximum (Δz^m), which depends on the width of a crack

$$\varepsilon_z^m(R,z) = \exp\left(-4\ \ln(2)\left(\frac{z}{\Delta z^m}\right)^2\right) \tag{12}$$

To solve the second derivative equation (equation (11)) with the given strain distribution (equation (12)) for the outer surface of the coating, additional straightforward boundary conditions are necessary. Considering the strain distribution around a crack tip, the first derivative of ε_z^f must be zero at the crack center, that is, the peak strain on the fiber appears at that point. Additionally, ε_z^f converges to zero far from the crack in the case of distributed strain measurement. The original work of this article, described in the following sections, combines with the above-mentioned principle to develop a methodology, as shown in Figure 2, for transferring strain information for a host material to measurement information.

Fiber-protective slippage. To make the methodology shown in Figure 2 more general and practical, the nonlinear slippage behavior of the surrounding components has to be considered. In larger cracks, experience shows that interfacial slippage between the fiber core and the surrounding material usually occurs as shown in Figure 3. A number of studies have been carried out to develop an interfacial stress–strain response (shown in Figure 4), and the following response is supposed to express the debonding behavior based on the simple assumption that the surrounding material softens suddenly once the stress reaches the maximum strength of the material, that is, the strain reaches the maximum bearing strain, $\varepsilon_z^{\max}$, corresponding to the sudden softening in Figure 4.[11] After this point, an increase in crack width causes an increase in the debonded region, because only the bonded region bears tensile stress. Therefore, the debonding considers the strain on the fiber, $\varepsilon_z^{f\ Deb.}(z)$, and can be categorized using the following two expressions, according to the strain at the crack center, $\varepsilon_z^f(0)$

$$\left\{\varepsilon_z^{f\ Deb.}(z) = \varepsilon_z^f(z) \quad \text{if } \varepsilon_z^f(0) \leqslant \varepsilon_z^{\max}\right. \tag{13}$$

$$\left\{\begin{array}{ll} \varepsilon_z^{f\ Deb.}(z) = \varepsilon_z^{\max} & z \leqslant z^{Deb.} \\ \varepsilon_z^{f\ Deb.}(z) = \varepsilon_z^f\left(z - z^{Deb.}\right) & z > z^{Deb.} \end{array}\right. \quad \text{if } \varepsilon_z^f(0) \geq \varepsilon_z^{\max} \tag{14}$$

where $\varepsilon_z^{\max}$ is the maximum strain and appears as the strain at the beginning of the debonding ($z = z^{Deb.}$).

The parameter $\Delta z_{ini.}^m$ can be considered to be the crack width when debonding is initiated. Since an increase in the crack width corresponds to an equal increase in the integrated strain in the debonded region, the following expression can be derived using the applied displacement (Δz^m) and the maximum strain ($\varepsilon_z^{\max}$) as the restraint conditions to solve $z^{Deb.}$ (in the case of $\varepsilon_z^f(0) \geq \varepsilon_z^{\max}$, see equation (14))

$$2 \cdot z^{Deb.} \cdot \varepsilon_z^{\max} = \Delta z^m - \Delta z_{ini.}^m \tag{15}$$

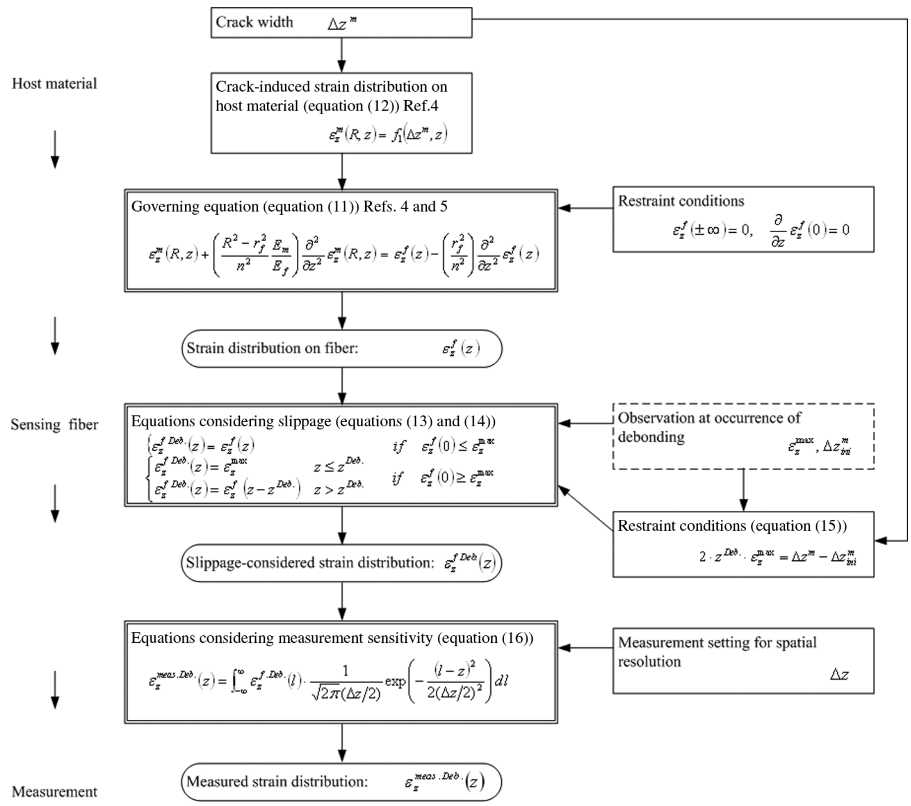

Figure 2. Methodology for analytical strain distribution in the case of a crack.

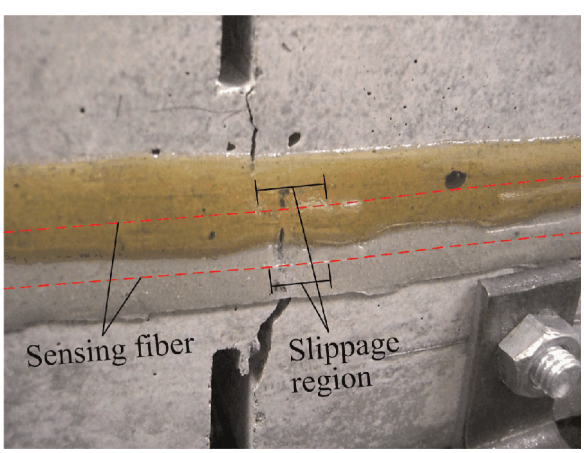

Figure 3. Interfacial slippage between fiber and surrounding materials.

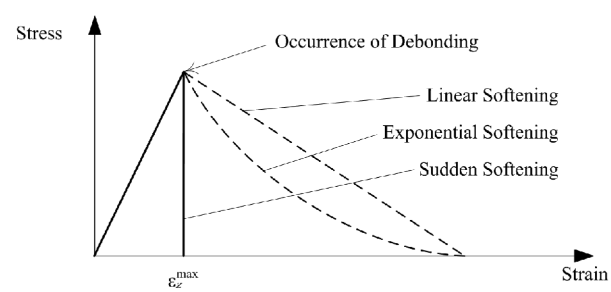

Figure 4. Stress–strain responses.

It should be noted that the maximum strain on the fiber, ε_z^{max}, and the corresponding crack width, $\Delta z_{ini.}^m$, have to be experimentally determined beforehand. In this study, an additional tensile test was conducted to observe such values in the same manner as the tensile test described in the following chapter. When debonding at the crack tip was first observed by a microscope during the preliminary test, $\Delta z_{ini.}^m$ was determined by microscopic measurement. In addition, ε_z^{max} was measured by the attached optical fiber sensor when there was a constant strain at the debonded region. Accordingly, the value of $z^{Deb.}$ was defined in equation (15) with an observed crack width of Δz^m. Depending on the bond strength of the surface between the surrounding material and the fiber, these values vary at different installation settings. Table 1 contains the results observed in the fixed and flexible settings.

Figure 5 depicts the numerical results for the strain distribution on the fiber calculated by using equations (13) and (14) with various crack widths, Δz^m, with equation (12). Position is normalized by the spatial resolution of measurement. In Figure 5, it is easily observed

Table 1. Analytical setting

Settings	Young's modulus and radius of fiber segment	Young's modulus and radius of component segment	Poisson's ratio of components	Shear-lag parameter	Observed crack width at initial debonding and maximum strain	Spatial resolution
	E_f, r_f	E_m, R	ν_m	n	Δz_{ini}^{m}, $\varepsilon_z^{\max}$	Δz
Fixed	72 GPa, 62.5 μm	0.5 MPa, 500 μm	0.3	0.0016	340 μm, 1230×10^{-6}	38 mm
Flexible	72 GPa, 62.5 μm	0.2 MPa, 1500 μm	0.3	0.0008	470 μm, 1340×10^{-6}	38 mm

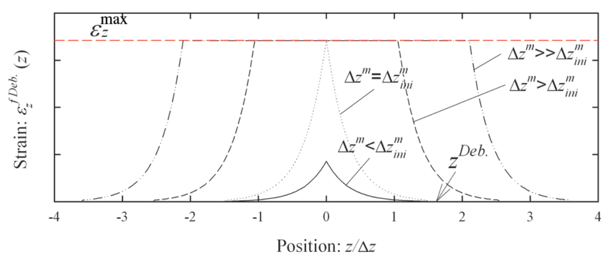

Figure 5. Analytical examples of strain distribution on fiber around a crack.

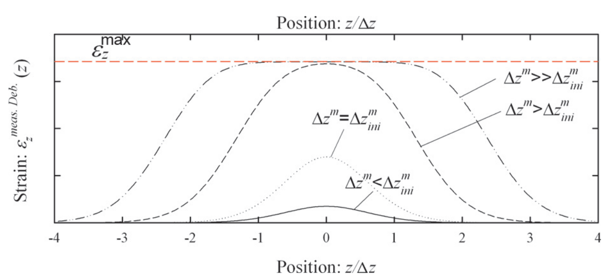

Figure 6. Analytical examples of strain distribution measured around a crack.

that a larger crack width expands the debonded area once the strain at the crack tip exceeds the maximum strain, $\varepsilon_z^{\max}$. Figure 5 assumes, of course, that the strain distribution in the debonded area is constant as a result of the fiber-protective slippage, because no load is transferred into the surrounding materials at that point because of perfect debonding.[11]

Sensor's sensitivity. The observed optical fiber sensor signal is intrinsically affected by the entire range of spatial resolution. Therefore, the sensor may lose some information if a constant strain distribution is not in place. As expressed in equation (16), it is assumed that the signal sensitivity of the distributed optical fiber sensor has a normal distribution with a certain standard deviation that corresponds to half the spatial resolution, Δz. Substituting equations (13) and (14) into equation (16), Figure 6 is obtained, which provides a numerical example of the measured strain distribution. It numerically expresses the behavior of the surrounding material and the limited spatial resolution at the crack tip on the host structure. Particularly, the limited spatial resolution results in indistinct strain distribution when compared with Figure 5.

$$\varepsilon_z^{meas.\,Deb.}(z) = \int_{-\infty}^{\infty} \varepsilon_z^{f.Deb.}(l) \cdot \frac{1}{\sqrt{2\pi}(\Delta z/2)} \exp\left(-\frac{(l-z)^2}{2(\Delta z/2)^2}\right) dl \qquad (16)$$

To apply equations (1) to (16) for crack identification, values of several parameters for the fiber setting are needed. In this study, two types of settings, fixed and flexible, are considered. The material properties and geometry of the analytical setting are depicted in Table 1 and refer to the study by Wan et al.[5] in terms of Young's modulus for the fiber segment. Young's modulus of the component is reduced for use in this study based on the proportional value of the model and the actual sectional area. The fiber segment is considered as being composed of optical fiber core and cladding, and the composite segment is considered to be similar to other surrounding materials such as the fiber-protective and fiber-adhesive materials. The observed crack width and maximum strain are also shown in Table 1. The fixed setting indicates the case in which the bare sensing fiber coated with a ultraviolet (UV)-protective material (250 μm in diameter) is directly installed onto the host structure using two composite epoxy adhesives, and the flexible setting indicates the case in which the UV-coated sensing fiber is installed onto a buffering rubber material embedded in the host material by the same epoxy adhesives. This buffering rubber material is used to decrease the strain sensitivity.

Experimental work

Experimental setup

To evaluate our developed numerical model, a tensile test was conducted on a mortar prism. The size of the specimen was 100 mm in height, 100 mm in width, and

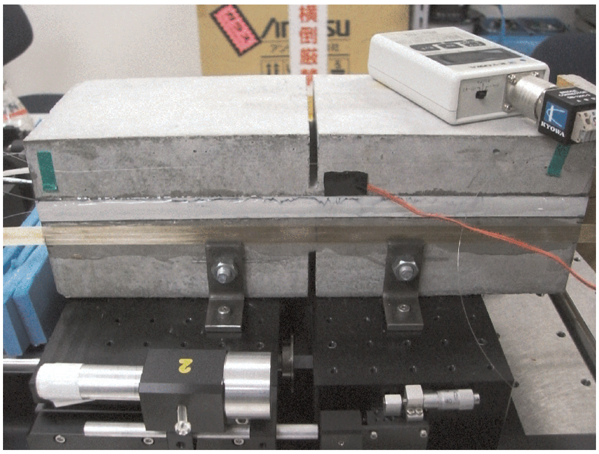

Figure 7. Experimental setup.

300 mm in length. To increase its ductility, plastic fibers were mixed with the concrete specimen. Notches were made (5 mm wide and 30 mm deep) at the top and bottom of the center of the specimen to induce a crack. In addition, reinforcing bars were embedded into the specimen to give a structural hold for the test equipment. The prisms, placed on the equipment, were gradually pulled to induce a crack, as illustrated in Figure 7. Precise capacitance sensors were used for a displacement control tensile test. The applied force and loading rate were not measured, as they were not of concern for this study.

The sensing fibers were installed on the surface of the prisms in two separate ways to simulate the two types of settings, fixed and flexible, described earlier. Figure 8 shows a sectional plan of the installed sensing fibers.[5]

While the gradual tensile force was being applied, the crack width was observed by a microscope (as shown in Figure 9), while the strain distribution was measured by the BOCDA-based optical fiber sensor.[12] In this case, the measurement was conducted at a spatial resolution of 38 mm and a measurement interval of approximately 10 mm.

Strain-distribution measurement for crack identification

The measurements from the optical fiber sensor and the calculated results for the fixed and flexible settings are shown in Figure 10(a) and (b), respectively, showing the strain distribution around the crack tip. The zero position corresponds to the crack center. Generally, it can be observed that the measurement is in good agreement with the numerical results, and hence it is confirmed that the proposed strain-transferring model is able to identify the crack. Figure 10 also indicates that the fixed setting is more sensitive than the flexible setting, and the affected area of the fixed setting is smaller than that of the flexible setting. It implies that the flexible surrounding components lead to lower measurement sensitivity, while the measurement is more robust in the harsher environment because of the added protection.

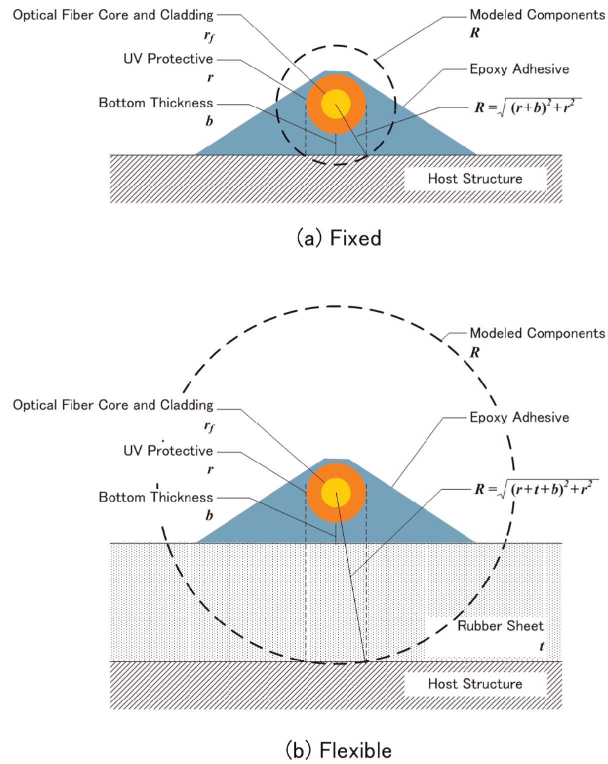

Figure 8. Cross-sectional diagram of installation setting: (a) fixed and (b) flexible.

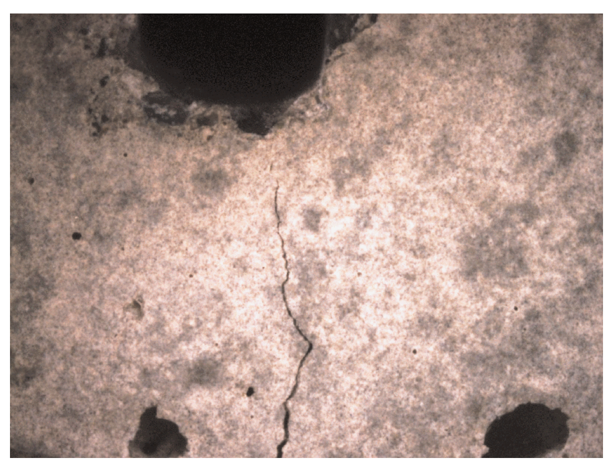

Figure 9. Microscopic photograph of a tiny crack.

For larger cracks in particular (for example, the 1380 μm crack in Figure 10(a)), there are large

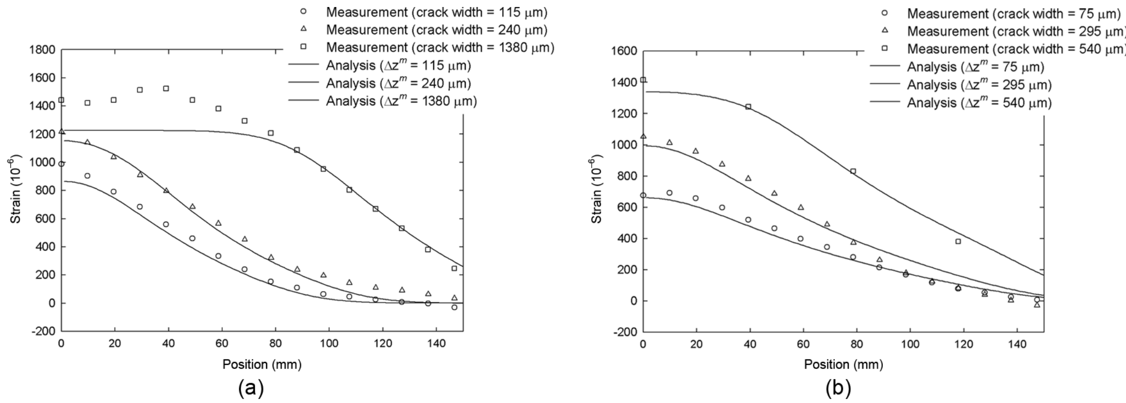

Figure 10. Measured and calculated strain distribution: (a) fixed setting and (b) flexible setting.

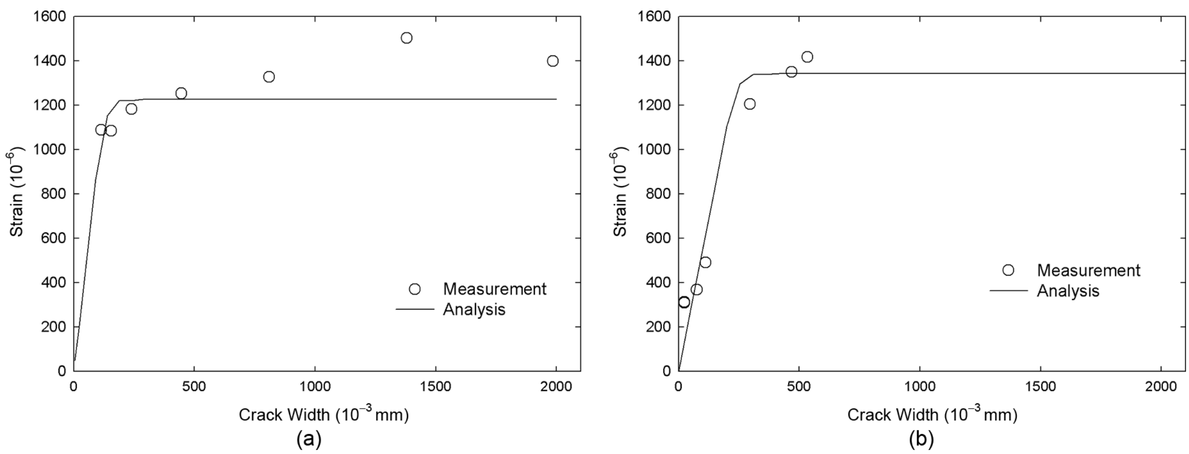

Figure 11. Measured and calculated strain at the crack tip: (a) fixed setting and (b) flexible setting.

discrepancies between the measurement and the numerical result. It is thought that the differences are derived from both the local invisible debonding and the tensile equipment, thus not compromising on the proposed model. A similar phenomenon was observed in a single-shear test on a fiber-reinforced plastic (FRP)–concrete specimen with very local invisible debonding at higher loading.[13] Because a perfect tensile loading could not be achieved with tensile equipment, an additional strain induced by slight bending might occur for a larger crack.

The collapse of the specimen occurred instantaneously with the growth of the crack in these tests owing to the extra spring force of the equipment; thus, the measurement had to be made very rapidly during crack growth. In the BOCDA-based sensor, the measurement time depends on the number of measurement points. Although the highly dense measurement was mainly conducted in the test, the number of measurement points was reduced to shorten the measurement time for one of the larger cracks (540 μm), as shown in Figure 10(b).

By focusing on the strain at the crack center, the measurement by the BOCDA-based sensor can be compared with the numerical results, as shown in Figure 11(a) and (b). Both are in reasonable agreement, and thus, it is also confirmed that the model is appropriate for evaluation of sensing fiber installation in terms of sensitivity and repeatability. As a sensor's sensitivity indicates the slope of the line at a smaller crack width in Figure 11(a), a fixed setting provides a higher sensitivity. As a sensor's repeatability indicates the linear range in Figure 11(b), a flexible setting provides a wider repeatability. The sensor will lose repeatability and residual strain will occur once the crack width exceeds a certain value (out of the linear range). For instance, monitoring on an aging crack requires sensitivity rather than repeatability, because the crack width might be monotonically opening. Monitoring a crack subjected to a variable force, for example, wind or traffic loading,

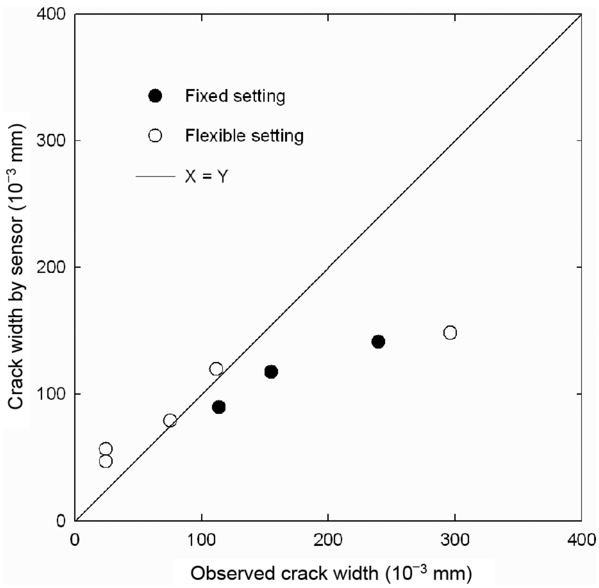

Figure 12. Comparison between observed crack width and estimated crack width by sensor.

generally requires repeatability rather than sensitivity, because the crack width might be repeatedly opening and closing.

According to numerical results, once the strain on the crack center reaches the maximum bearing strain, ε_z^{max}, the measured strain on the crack remains constant. However, owing to the reasons mentioned earlier—local invisible debonding at the crack tip and the inability to produce perfect tensile loading—the strain exceeds the maximum bearing strain with larger cracks, as shown in Figure 11(a).

In considering the accuracy of BOCDA-based sensors (approximately 100×10^{-6}), it is assumed that the minimum detectable crack is approximately 10 μm for the fixed setting, because this is when the analytical result trend reaches 100×10^{-6}. This value is consistent with the results from a previous experimental observation.[14] Furthermore, it is assumed that the minimum detectable crack is approximately 20 μm for the flexible setting.

Figure 12 shows the relationship between the crack width from the distributed strain obtained from the stimulated BOCDA and the corresponding measured crack width by a microscope. To estimate the crack width, the measured strain distribution is integrated in the range of the specimen. It should be noted that Figure 12 shows that the results are less than 400 μm in crack width. Larger crack-induced strain reaches over the edge of the specimen; however, the strain was measured within the specimen. Therefore, the error cannot be ignored in the case of a larger crack. Referring to Figure 10(a) and (b), the strain at the edge of the specimen (150 mm in position) is more than zero at the crack, over 300 μm approximately, which can be defined as the maximum crack width for model evaluation by this size of specimen. In Figure 12, although slight bending on the specimen might result in some discrepancies, the plots show that an appropriate estimation is accomplished.

Summary

To express the transfer of stress from a host structure to a sensing fiber, a model (based on a stress-equivalent model) incorporating drastic softening behavior for the surrounding components is proposed for the purpose of crack identification using a stimulated Brillouin-based sensor. The maximum strain on the fiber and the debonding-initiated crack width is initially determined experimentally, and the strain distribution change resulting from the crack is then calculated using the proposed model. The analyzed strain distribution is recalculated using a Gaussian-shaped signal sensitivity. The model is confirmed by experimental results using different sensing fiber installations, and these installations are able to control the sensitivity for crack identification, while also being repeatable. The fixed-setting installation type, in particular, provides a higher sensitivity, though the flexible-setting installation type provides a higher repeatability because of lesser fiber-protective slippage.

Funding

This research received no specific grant from any funding agency in the public, commercial, or not-for-profit sectors.

References

1. Li D, Li H, Ren L, et al. Strain transferring analysis of fiber Bragg grating sensors. *Opt Eng* 2006; 45(2): 024402-1–024402-8.
2. Hameed A, Fernando GF, Hetherington JG, et al. Investigation of strain transfer to a sensor protection system embedded in concrete using finite element analysis. *Mater Struct* 2002; 35: 557–563.
3. Ansari F and Libo Y. Mechanics of bond and interface shear transfer in optical fiber sensors. *J Eng Mech* 1998; 124(4): 385–394.
4. Duck G and LeBlanc M. Arbitrary strain transfer from a host to an embedded fiber-optic sensor. *J Smart Mater Struct* 2000; 9(4): 492–497.
5. Wan KT, Leung CKY and Olson NG. Investigation of the strain transfer for surface-attached optical fiber strain sensors. *J Smart Mater Struct* 2008; 17(3): 1–12.
6. Ohno H, Narusa H, Kihara M, et al. Industrial applications of the BOTDR optical fiber strain sensor. *Opt Fiber Technol* 2001; 7(1): 45–64.

7. Inaudi D and Glisic B. Reliability and field testing of distributed strain and temperature sensors. *Proc SPIE Smart Struct Mater* 2006; 6167: 61671D1–61671D8.
8. Lanticq V, Quiertant M, Merliot E, et al. Brillouin sensing cable: design and experimental validation. *IEEE Sens J* 2008; 8(7): 1194–1201.
9. Duck G, Renaud G and Measures R. The mechanical load transfer into a distributed optical fiber sensor due to a linear strain gradient: embedded and surface bonded cases. *J Smart Mater Struct* 1999; 8(2): 175–181.
10. Cox HL. The elasticity and strength of paper and other fibrous materials. *Br J Appl Phys* 1952; 3(3): 72–79.
11. Lu XZ, Teng JG, Ye LP, et al. Bond-slip models for FRP sheets/plates bonded to concrete. *Eng Struct* 2005; 27(6): 920–937.
12. Hotate K and Hasegawa T. Measurement of Brillouin gain spectrum distribution along an optical fiber using a correlation-based technique: proposal, experiment and simulation. *IEICE Trans Electron* 2000; E83-C(3): 405–412.
13. Yao J, Teng JG and Chen JF. Experimental study on FRP-to-concrete bonded joints. *Composites Part B* 2005; 36(2): 99–113.
14. Imai M, Nakano R, Kono T, et al. Crack detection application for fiber reinforced concrete using BOCDA-based optical fiber strain sensor. *J Struct Eng* 2010; 136(8): 1001–1008.

Appendix 1

Nomenclature

E_f	Young's modulus of the fiber
E_m	Young's modulus of the surrounding material
G_m	Shear modulus of the surrounding material
n	Shear-lag parameter
r_f	Radius of the fiber
R	Radius of the surrounding material
u^m	Longitudinal displacement of the surrounding material
ω^m	Transverse displacement of the surrounding material
$z^{Deb.}$	Beginning position of the debonding

Greek letters

Δz	Half of the spatial resolution of the sensor
Δz^m	Full width at half maximum (depends on the width of a crack)
$\Delta z^m_{ini.}$	Crack width when debonding is initiated
$\bar{\varepsilon}^f_z$	Mean axial strain on the fiber
$\bar{\varepsilon}^m_z$	Mean axial strain on the surrounding material
ε^f_z	Axial strain on the fiber
ε^m_z	Axial strain on the surrounding material
$\varepsilon^{\max}_z$	Maximum bearing strain
$\varepsilon^{f\,Deb.}_z$	Axial strain on the fiber considering the debonding
$\varepsilon^{meas.\,Deb.}_z$	Measured strain on the fiber considering the debonding
ν_m	Poisson's ratio of the surrounding material
$\bar{\sigma}^f_z$	Mean normal stress on the fiber
$\bar{\sigma}^m_z$	Mean normal stress on the surrounding material
τ^f_{rz}	Shear stress on the fiber
τ^m_{rz}	Shear stress on the surrounding material